Multi-length Scale Microstructural Design of Micro-tubular Solid Oxide Fuel Cells for Optimised Power Density and Mechanical Robustness

Xuekun Lu[1,2*], Antonio Bertei[3,4], Thomas M.M. Heenan[1], Yunsong Wu[1], Dan JL Brett[1], Paul R Shearing[1]

[1]Electrochemical Innovation Lab, Department of Chemical Engineering, University College London, London, WC1E 7JE, UK

[2]National Physical Laboratory, Hampton Road, Teddington, Middlesex TW11 0LW, UK

[3]Department of Earth Science and Engineering, Imperial College London, London, SW7 2AZ, UK

[4]Department of Civil and Industrial Engineering, University of Pisa, Pisa, 56122

Abstract

In this study, we aim to parametrically reveal the dependence of electrochemical performance on a variety of microstructural characteristics at multi-length scale in a micro-tubular solid oxide fuel cell to shed light on the advanced electrode design. Numerical Direct Simulation Monte Carlo methods are used on the tomographically-reconstructed 3D microstructure of the anode to characterise the tortuosity factors as a function of the porosity and pore diameter accounting for the Knudsen flows. These are subsequently incorporated in the mass transport in 2D electrochemical simulations. Results show that the Knudsen tortuosity factor is two times larger than that estimated by the continuum physics. High substrate porosity and pore size show unnoticeable effect in facilitating the mass transport provided that the micro-channels span over 60% of the radial thickness. The width and radial distribution of the micro-channels have little influence on the mass transport, but the compactness greatly affects the global performance. Optimal designs are identified as i) 80% micro-channel length and 27% substrate porosity to reach maximum power density (1.18 W cm^{-2}) with

*Corresponding author: Electrochemical Innovation Lab, Department of Chemical Engineering, University College London, London, WC1E 7JE Email: xuekun.lu@ucl.ac.uk

lowered mechanical strength, or ii) 60% micro-channels length and 27% porosity to obtain a more balanced performance (0.96 W cm^{-2}) with better long-term structural integrity.

Keywords: anode microstructure, Knudsen diffusion, tortuosity factor, micro-channels, triple phase boundary, mass transport

1. Introduction

In recent years, a vast majority of laboratory and modelling effort have been focused on improving the performance of existing energy systems via microstructural optimisation as well as exploring new types of sustainable energy sources [1-3]. Solid Oxide Fuel Cells (SOFCs) are one of the most promising candidates of next generation electrochemical devices due to the fuel flexibility, low emissions and high efficiency. The present development of SOFCs is focused on two major designs which can be classified as planar and tubular geometric configurations. The tubular type provides better thermal-cycling resistance, simpler gas sealing and a broader variety of manufacturing technologies [4, 5]. In addition, reducing the diameter of the tubular SOFCs (so called micro-tubular designs) can potentially increase the volumetric power density as well as thermal shock resistance [6], which is especially beneficial to decrease the start-up time.

Generally, anode-supported tubular SOFCs are the most popular design compared to the electrolyte-supported and cathode-supported ones to pursue low ohmic resistance and fabrication convenience. In recent years, traditional extrusion techniques have been typically used to fabricate the substrate tubes. However, anodes with this symmetrical structure show a large concentration polarization due to the sluggish mass transport in the tortuous gas pathways in the anode substrate [7-9], which significantly undermines the electrochemical performance, especially at high current density. Large pore contributes to favorable mass transport properties, but results in less balanced microstructural morphology thus lower triple phase boundary (TPB) for electrochemical reaction [10] and could also

affect the mechanical strength; for applications prioritising long-term operation and mechanical integrity, lower porosity and pore size are advantageous but could lead to significant concentration polarization. Understanding the interplay between microstructures and performance is critical in guiding the materials manufacturing for different energy applications.

Exploring new forms of sustainable energy systems has attracted broad interest. Hierarchical porous structures are regarded as the prospective option to address this problem. Recently an immersion induced phase-inversion extrusion technique [11-15] has been introduced to fabricate micro-tubular SOFCs (MT-SOFC) with an asymmetric hollow fiber structure that can markedly improve the mass transport in the substrate. Compared to conventional tubular SOFCs, which consist of the symmetric sponge-like porous anode (pore diameter 0.2 μm), SOFCs fabricated by this technique are incorporated with radially grown micro-channels (diameter 10~20 μm) from the inner wall of the anode tube because of the exchange process between solvent and non-solvent [16, 17]. This hierarchical pore design can considerably facilitate the mass transport while maintaining a high mechanical strength and long-term stability.

The most important advantage of the phase-inversion technique in the MT-SOFC fabrication is the flexibility of microstructure design and optimisation procedures, which have historically been the key technical challenges to improve the electrochemical performance. Previous studies have successfully managed to fabricate MT-SOFCs with different micro-channel morphologies and relate them to the mechanical strength and gas permeance [16, 18]. It was found that longer and larger micro-channels significantly enhance the mass transport, but at the cost of mechanical strength. Apart from the micro-channels, spongy substrates of different porosities and pore sizes can also be achieved by the addition of pore formers in the suspension [19] and by varying the sintering temperature [20, 21]. Higher porosity and larger pore diameter in the spongy substrate greatly improve the electrochemical performance, but the flexure strength and long-term mechanical stability are undermined.

Despite the recent progress in MT-SOFC fabrication and structural optimisation, the relationship of microstructure and the performance at different length scales remains to be elucidated. Three main material characteristics will be the focus this study: 1) micro-channels; 2) pore diameter in the spongy substrate; 3) porosity. All of them are closely related to the mass transport process, but under different flow physics: micro-channels act as a fast track driving the gas reactant from the center bore towards the reacting sites due to the low resistance. Mass transport in this region is governed by viscous flow under continuum flow regime (Knudsen number $Kn << 0.1$); in contrast, the pore diameter in the spongy substrate is significantly smaller than the micro-channels (0.2 *vs.* 20 μm) and comparable to the mean free path of the gaseous reactant ($1 < Kn < 5$, transition flow regime) [22], thus the molecule/wall collisions (Knudsen effect) cannot be ignored. The mass flow is governed by both viscous and Knudsen flow and the diffusivity is significantly lower than that in the micro-channels. The change of pore diameter, in essence, is shifting the relative ratio between viscous and Knudsen flow; the porosity is regarded as an effective mass transport parameter of the spongy substrate. In theory, the diffusive mass flux is linearly proportional to the porosity, but higher porosity increases the percolation ratio and decreases the tortuosity factor of the mass transport pathways, which could improve the diffusive mass flux exponentially. Apart from mass transport, the porosity also affects the TPB density in terms of percolated TPB, solid phase interface, and solid phase percolation [10]. In a summary, performance optimisation requires a trade-off between mass transport, reaction rate and mechanical strength of the MT-SOFC. Thus, towards practical structural design, the fundamental insights allow us to suggest specific strategies for different applications.

The 3D microstructure of the MT-SOFC can be investigated using non-destructive X-ray computed tomography (X-ray CT), which reconstructs the materials according to their distinct X-ray attenuation coefficients [23, 24]. The mass transport parameters in the spongy substrate can be obtained using image-based modeling on the reconstructed transport pathways. In the spongy substrate, the mass transport parameter for the viscous flow is normally obtained using continuum computational fluid dynamics (CFD) [17, 25] while few efforts have been made to quantify the effective diffusivity

accounting for the Knudsen effect (non-continuum) based on the reconstructed 3D microstructure. When Knudsen effect is involved, continuum fluid dynamics (Navier-stokes equation) cannot accurately describe the mass flow in the porous medium anymore. The Direct Simulation Monte Carlo (DSMC) method has become a powerful tool to simulate the rarefied gas flows and has been employed by a number of other works to model flow through a variety of porous media, such as fibrous materials [26-28], ablative materials [29] and channels filled with packed spheres [30, 31]. This method has been well validated by comparing the numerical simulation either with the experimental permeability [29] or the established analytical solution [26]. However, few attempts have been made to apply these methods to the reconstructed 3D microstructure of SOFC electrodes to extract the effective diffusivity accounting for molecule/surface collisions. Instead, random packing sphere models generated are more often used as a replacement for the electrode to conduct the theoretical diffusivity investigation [32-34]. These algorithm-based morphologies are less representative of the typical 3D porous pathways and the roughness of the particle surface in the electrode than the reconstructed 3D volume.

This study will be a significant extension building on our previous study which presented the developed methodology in the extraction of Knudsen mass transport parameters using DSMC technique [35]. Here, we aim to integrate this methodology for the first time to elucidate the interplay of electrochemical performance of MT-SOFCs, with the multi-length scale microstructural characteristics, such as size, percolation, compactness and radial distribution of the macroscopic micro-channels, as well as local pore size/porosity and tortuosity in the spongy substrate. In anode substrate, the effective mass transport parameter as a function of the porosity and pore diameter is quantified using image-based modeling for the reconstructed 3D microstructure, which will then be incorporated in the electrochemical performance simulation. We believe this study can provide new strategy of rationalising the microstructural design of the MT-SOFC anode, suggesting the optimal microstructure characteristics as a balance between the reaction kinetics, mass transport and mechanical strength. The methodology introduced in this work is widely applicable to other energy

materials which are also manufactured with hierarchical microstructures, such as batteries, membranes and catalysts.

2. Material and Methods

The MT-SOFC sample was previously fabricated using phase inversion technique. The detailed information of the material preparation procedure and the scanning parameters of the multi-scale X-ray computed tomography (X-ray CT) can be found here [36]. Fig. 1 demonstrates the workflow of this study linking multi-scale X-ray CT and modelling.

The segmented pore volume of the spongy substrate was then directly used as the flow domain simulated using Avizo Xlab Diffusion (Thermo Fisher Scientific, USA) to measure the tortuosity factor τ_c for the continuum flow and effective mass transport parameter ε/τ_c using ordinary H_2 flow simulation (Fig. S1). The boundary condition was set so that there is a concentration gradient of 1 mol m^{-3} between the inlet and outlet.

For the Knudsen mass transport parameters, the segmented pore volume was imported to the open source SPARTA software [38] to conduct Direct Simulation Monte Carlo (DSMC) simulation. Subsonic boundary condition was defined for the counter-diffusion of H_2/H_2O binary mixture (inlet H_2, outlet H_2O, 800 ℃, 1 bar). 20 million molecules were initialised in a solution domain of 260 μm^3 consisting 3.5 million grids so that at least 20 simulating particles were included in each grid to avoid statistical scattering [39, 40]. In DSMC, each of these simulating molecules is regarded as the representative of a large number of real molecules that have the identical properties such as temperature, velocity so that the computational load is greatly reduced compared to other molecular modelling methods such as molecular dynamics simulation (MD). The number of real molecules per simulating particle is known as scaling factor (*fnum* in SPARTA) and the simulated gas state parameters such as pressure and flux in each grid by simulating particles are multiplied by *fnum* to represent the real physical

state. Generally the higher the *fnum*, the less reliable the result is, especially for high Knudsen number condition. In this study, a scaling factor of 18 was used and small enough to provide accurate DSMC results [40]. The equations for Knudsen tortuosity factor and apparent permeability calculation can be found from Section 2 in Supplementary Information.

3. Electrochemical Simulation

The reconstructed full cell micro-CT scan and spongy anode nano-CT scan were then segmented and visualised in 3D (Fig. 1e and f). Parametric studies of the electrochemical performance as a function of macroscopic material characteristics (i.e. micro-channels width, length, density by micro-CT) and microscopic material characteristics (i.e. anode porosity, pore size, tortuosity factor, TPB density by nano-CT) was conducted on a 2D geometric configuration thanks to the axial symmetry of the MT-SOFC (Fig. 1g). Due to high inner to outer radii ratio of the cell (∼0.8), model equations are framed in planar form instead of axial-symmetric form as the discrepancy of mass flow rate between the two cases is insignificant [41]. The radially-aligned micro-channels further support the validity of this model simplification. The knowledge of electrode design obtained from this study is potentially also applicable to planar SOFC electrodes with embedded micro-channels. Segmented spongy substrate volume (Fig. 1c) was used to conduct the CFD simulation to extract the tortuosity factor (Fig. 1h), which was then used to define the effective diffusivity of the substrate in the electrochemical simulation.

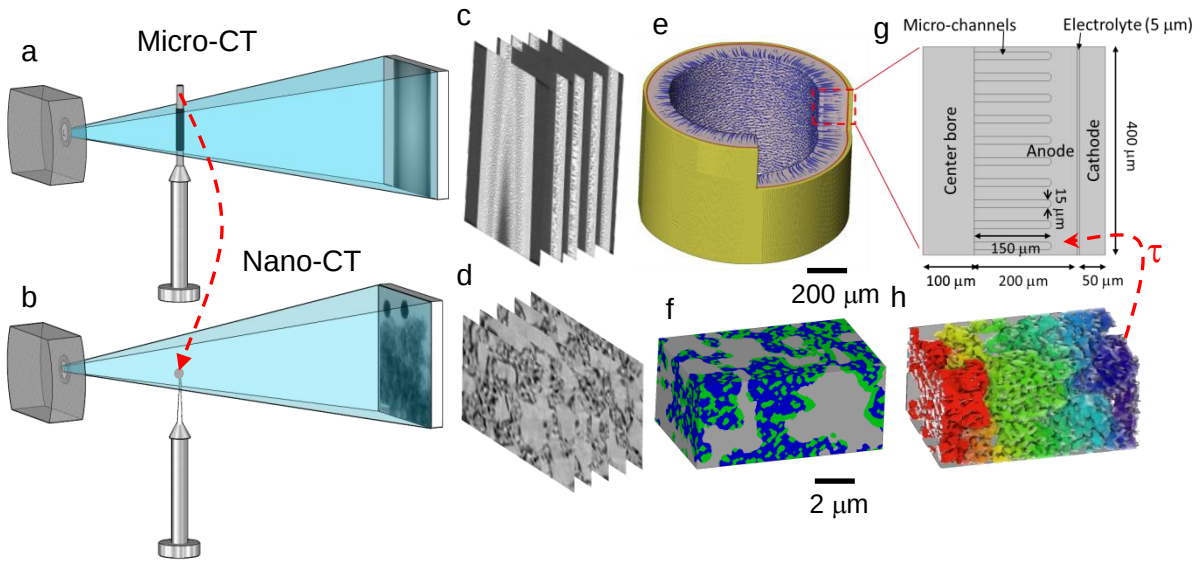

Fig. 1 Illustration of the workflow in this study: (a) schematic of micro-CT set-up and (b) nano-CT set-up. It is noted that this is a simplified schematic without showing the optics in the CT systems. (c) Reconstructed slices of the full cell (grey: anode substrate; black: pore) and (d) spongy anode substrate (light grey: YSZ; dark grey: Ni; black: pore); (e) 3D volume rendering of the segmented MT-SOFC (blue: micro-channels; grey: anode substrate; red: electrolyte; yellow: cathode); (f) 3D volume rendering of the segmented spongy anode (grey: YSZ; blue: Ni; green: pore); (g) the simulation geometry as part of the axial cross section, with the geometrical sizes defined according to the micro-CT analysis; (h) concentration gradient of the diffusion simulation on the pore phase of the segmented volume in (f) and the extracted effective diffusivity was used to define the 2D simulation model in (g).

Charge balance, mass conservation, species conservation, and momentum conservation were enforced in the solution domain. The balance for a species (e.g. gas and charge species), either consumed or produced in the electrochemical reaction process at the TPB, is expressed in the whole simulation domain in molar basis depending on the stoichiometric coefficients ν_s as follows:

$$\nabla \cdot J_s = \frac{\nu_s}{\nu_e} \frac{i\lambda^{TPB}}{F} \quad (s = H_2, H_2O, e^-, O^{-2}, O_2, N_2) \tag{1}$$

where J_s represents the molar flux of the species (mol m^{-2} s^{-1}), v_e the electron transfer number, i the current density per unit TPB length (A m^{-1}), λ^{TPB} the TPB density (m^{-2}) and F the Faraday constant.

3.1 Transport in Channels

The advantage of MT-SOFC design is that the mass transport resistance has been significantly reduced by the radially aligned micro-channels, which serve as highways to transport the reactant gas to the reaction sites and adjacent anode substrate by permeation. The gas transport in micro-channels is represented by continuum flow due to the large size of the micro-channels as the molecule-wall interaction can be safely neglected. The mass transport in the cathode can also be treated as continuum flow as the Knudsen effect is insignificant compared to the anode due to the large molecular weight and small mean free path of the O_2/N_2 binary gas system, thus the flow is mainly governed by viscous flow. Both convection and diffusion fluxes are taken into account and represented by the first and second term respectively:

$$J_s = \frac{\rho}{M_s}\left(u w_s - D_c \nabla w_s\right) \quad (s = H_2,\ H_2O,\ O_2,\ N_2) \tag{2}$$

where D_c, w_s, ρ, R, T and u represent continuum diffusivity (m^2 s^{-1}), mass fraction of species s, mass density (kg m^{-3}), gas constant (8.314 J mol^{-1} K^{-1}), temperature (K) and mass-average velocity (m s^{-1}) of the fluid, respectively. The continuum diffusivity (cm^2 s^{-1}) in a binary system is calculated as [39, 40]:

$$D_c = \frac{10^{-3} T^{1.75}}{P(V_{s1}^{1/3} + V_{s2}^{1/3})^2}\{\frac{1}{M_{s1}} + \frac{1}{M_{s2}}\}^{0.5} \quad (s1,\ s2 = H_2 / H_2O \text{ or } O_2 / N_2) \tag{3}$$

where $V_{s1,s2}$ means the Fuller diffusion volume for the species: H_2 (7.07), O_2 (16.6), N_2 (17.9) and H_2O (12.7) [42], $M_{s1,s2}$ represents the molecular weight (g mol^{-1}) and P the total pressure (bar). The momentum balance must also be ensured by Navier-Stokes equation with laminar flow condition:

$$\rho(u \cdot \nabla)u = -\nabla P + \nabla \cdot (\mu \nabla u) \tag{4}$$

where μ is the viscosity (Pa s). The viscosity was obtained using Herning and Zipperer method as [43]

$$\mu = \frac{y_{s1}\mu_{s1}\sqrt{M_{s1}} + y_{s2}\mu_{s2}\sqrt{M_{s2}}}{y_{s1}\sqrt{M_{s1}} + y_{s2}\sqrt{M_{s2}}} \tag{5}$$

The species viscosities can be calculated according to Todd and Young [43] as follows:

$$\mu_s = 10^{-7} \cdot \sum_{m=0}^{6} b_m \left(\frac{T}{1000} \right)^m \tag{6}$$

where b_m represents the factors of the best six-order polynomial fit which describes the dependence of viscosity on temperature.

3.2 Transport in the Anode Spongy Substrate

As transitional flow physics governs the mass transport in this region, a Knudsen-corrected dusty-gas model based on DSMC simulation is used to solve the gas flow for a binary gas mixture:

$$J_{s1} = -\frac{P}{RT}\alpha_{s1}^{-1}\nabla y_{s1} - \frac{y_{s1}}{RT}\left(\alpha_{s1}^{-1}\left(1 + \frac{D_{s2,k}^{eff}}{D_c^{eff}} \right) + \frac{kP}{\mu} \right)\nabla P \quad (s1,\ s2 = H_2, H_2O) \tag{7}$$

$$\alpha_{s1} = \frac{1}{D_{s1,k}^{eff}} + \frac{y_{s2}}{D_c^{eff}}\left(1 + \frac{y_{s1}}{y_{s2}}\sqrt{\frac{M_{s1}}{M_{s2}}} \right) \quad (s1, s2 = H_2, H_2O) \tag{8}$$

where $D_{s1,k}^{eff}$, and D_c^{eff} represent the effective Knudsen diffusivity and the effective continuum diffusivity. $D_{s1,K}^{eff}$ and D_c^{eff} can be obtained by the equations below:

$$D_k^{eff} = \frac{\varepsilon}{\tau_k} D_k \tag{9}$$

$$D_k = \frac{d_p}{3}\sqrt{\frac{8RT}{\pi M}} \tag{10}$$

$$D_c^{eff} = \frac{\varepsilon}{\tau_c} D_c \tag{11}$$

where τ_c stands for the tortuosity factor of the continuum flow, which is obtained by the continuum flow simulation in the spongy substrate as was introduced in Section 2. τ_k is the Knudsen tortuosity factor and is obtained by solving for $D_{s1,k}^{eff}$ in Eq. (7) by considering the molar fluxes obtained by numerical (DSMC) simulation. k is the permeability (m^2) obtained by the DSMC simulation which, notably, takes the wall slippage effect into account. Detailed descriptions can be seen in Supplementary Information.

3.3 Charge Transport

The charge transport in the ion conducting phase and electrical conducting phase follows Ohm's law

$$J_s = -\frac{\sigma_p^{eff}}{q_s F}\nabla V_p \quad (s = e, O^{2-}; p = an, ca, ele) \tag{12}$$

where q_s, σ_p^{eff} and V_p represent species charge, the effective conductivity (S m^{-1}) and the electric potential (V) in the specific phase p. The bulk conductivity σ_p is a function of temperature for each solid conductor [44-46]:

$$\sigma_{an} = 3.35\times10^4 \exp(\frac{-1392}{T}) \tag{13}$$

$$\sigma_{ca} = 1.23\times10^4 \exp(\frac{-600}{T}) \tag{14}$$

$$\sigma_{ele} = \frac{2.5\times10^7}{T}\exp(\frac{-9.8\times10^4}{RT}) \tag{15}$$

The effective conductivity is obtained by multiplying the bulk conductivity with the microstructure parameter [47]:

$$\sigma_p^{eff} = \frac{\phi_m}{\tau_m}\sigma_p \quad (p = an, ca, ele;\ m = el, io) \tag{16}$$

where ϕ_m and τ_m indicate the volume fraction and tortuosity factor of the conducting materials in phase *p*.

3.4 Reaction Kinetics

The Butler-Volmer equation is used to relate the generated current density (i_a, i_c) with the local activation overpotential (η_a, η_c) at anode and cathode respectively (Eq. (17) and Eq. (18)). The exchange current density per unit length of TPB (i_{a0}, i_{c0}) is coupled with the partial pressure of the reactant and product thereby the mass transport process [48, 49],

$$i_a = i_{a0}\left\{\exp\left(\frac{(1+\alpha_a)F\eta_a}{RT}\right)-\exp\left(\frac{-\beta_a F\eta_a}{RT}\right)\right\} \tag{17}$$

$$i_c = i_{c0}\left\{\exp(\frac{\alpha_c F\eta_c}{RT})-\exp(\frac{-\beta_c F\eta_c}{RT})\right\} \tag{18}$$

$$i_{a0} = i_{a0}^{ref}\exp\{-\frac{E_a^{act}}{R}(\frac{1}{T}-\frac{1}{T_a^{ref}})\}\frac{(\frac{P_{H_2}}{P_{H_2}^*})^{\frac{1-\alpha_a}{2}}(\frac{P_{H_2O}}{1.013\cdot 10^5})^{\frac{1+\alpha_a}{2}}}{1+(\frac{P_{H_2}}{P_{H_2}^*})^{0.5}} \tag{19}$$

$$P_{H_2}^* = \frac{A_{des}\Gamma^2\sqrt{2\pi RTM_{H_2}}}{\gamma_0}\exp(-\frac{E_{des}}{RT}) \tag{20}$$

$$i_{c0} = i_{c0}^{ref}\exp\{-\frac{E_c^{act}}{R}(\frac{1}{T}-\frac{1}{T_c^{ref}})\}(\frac{P_{O_2}}{P_{O_2}^{ref}})^{0.35} \tag{21}$$

The local activation overpotential (η_a, η_c) is calculated by subtracting the equilibrium potential difference ($V_{eq,a}$, $V_{eq,c}$) from the electronic and ionic potential difference as [50]:

$$\eta_a = \left(V_{ela}-V_{io}\right)-\Delta V_{eq,a},\ \Delta V_{eq,a} = -\frac{RT}{2F}\ln\left(\frac{y_{H_2}}{1-y_{H_2}}\right) \tag{22}$$

$$\eta_c = \Delta V_{eq,c}-\left(V_{elc}-V_{io}\right),\ \Delta V_{eq,c} = E_0+\frac{RT}{4F}\ln\left(Py_{O_2}\right) \tag{23}$$

where V_{ela}, V_{elc} and V_{io} represent potential of electric conducting phase in anode, cathode and ion conducting phase respectively. Notably, the local anodic concentration overpotential (η_a^{conc}) is equal to the difference in $V_{eq,a}$ values between operation and open circuit conditions. The sign convention used here is that both activation overpotentials (η_a, η_c) and current densities (i_a, i_c) are positive in fuel cell (Galvanic) mode.

3.5 Boundary Conditions and Input Parameters

The potential at the anode current collector was set to zero as a reference potential and the potential at the cathode current collector was set as cell operating voltage V_{cell} as

$$V_{cell} = OCV - V_{pol} \tag{24}$$

where OCV represents the open circuit voltage and V_{pol} is the polarization of the cell, which was set to sweep from 0 to 1.15 V. The center bore of the anode was fed with H_2 of 99% molar concentration with the flow rate of 30 mL/min to be consistent with the experiment. Air was used at the cathode. The input parameters for the developed model are listed in Table 1.

Table 1 Model input parameters for the anode and cathode respectively

Parameters	Value	Unit	Parameters	Value	Unit
Anode			Cathode		
i_{a0}^{ref}	4.1×10^{-2} [48]	A m^{-1}	i_{c0}^{ref}	2.5×10^{-4} [51]	A m^{-1}
λ_a^{TPB}	5.3	μm^{-2}	λ_c^{TPB}	4.6 [50]	μm^{-2}
E_0	0.98	V	α_c	1.5 [51]	
α_a	1.3 [48]	/	β_c	0.5 [51]	
β_a	0.7 [48]	/	E_c^{act}	1.4×10^{5} [51]	J mol^{-1}
E_a^{act}	1.2×10^{5} [52]	J mol^{-1}	T_c^{ref}	1218 [51]	K
T_a^{ref}	973 [48]	K	P_{O2}^{ref}	0.21 [51]	atm
A_{des}	5.59×10^{15} [53]	s m^2 mol^{-1}	ϕ_{el}	0.31	/

E_{des}	8.812×10^{4} [53]	J mol^{-1}	ϕ_{io}	0.33	/
Γ	2.6×10^{-5} [53]	Mol m^{-2}	ε_{ca}	0.36 [54]	
ϕ_{el}	0.39	/	τ_{el}	31 [50]	
ϕ_{io}	0.43	/	τ_{io}	8.5 [50]	
ε_{an}	0.19				
τ_{el}	4.31				
τ_{io}	2.12				

4. Result and Discussion

4.1 Multi-length Scale Microstructures and Effective Mass Transport Parameters

The macroscopic structure of the MT-SOFC anode is visualised in Fig. 2a, in which the 3D distribution of micro-channels at the inner wall, surface and internal substrate of the tube are clearly presented. The cross-sections of each individual micro-channel on a series of concentric layers are subsequently extracted via post-processing of the 3D reconstructed tomographic data in Matlab (Fig. 2b), so that the radial distribution of micro-channel diameter and volume fraction can be obtained (Fig. 2c). It is found that the diameter and volume fraction of the micro-channels monotonically decrease from the inner wall of the tube. The effective length of the micro-channels is approx. 150 μm (75% of the tube thickness), beyond which they fade dramatically. An average micro-channel size of 15 μm and the according number density (40 μm/channel) are used in the electrochemical simulation later. The 3D reconstruction of the spongy substrate of the anode is shown in Fig. 2d, in which the pore phase is rendered transparent.

Generally, gas flow in most of the SOFC anodes is classified as the transitional flow regime due to the comparable pore size and mean free path of the reactant gas, both viscous (continuum flow) and Knudsen fluxes (non-continuum flow) contribute to the mass transport process. Fig. 2d shows the H_2 flow streamlines obtained from H_2 diffusion simulated on the pore network in the spongy anode

substrate according to continuum flow. Pore constrictions are noted, represented by the local maxima of the mass flux. This morphological feature is also regarded as a cause of mass transport limitation and its effect can be integrated in the continuum tortuosity factor (τ_c), which is obtained by comparing the diffusive flux with the one simulated in an empty volume using continuum flow physics (for more details see Section 1 in SI).

To highlight the impact of inter-molecular interactions and molecular-wall collisions, the Knudsen tortuosity factor τ_k was extracted by the numerical DSMC method so that it can be compared with the continuum one as obtained above. Although this method has been well validated either experimentally [29] or through the established analytical solution [26], this study used a gas permeation experiment to examine the consistence between the simulation and experiment for different gases under a range of pressures (for more details about the experiment setup and validation, see Section 5 in SI).

Fig. 2e demonstrates a snapshot of the counter-diffusion of a binary H_2/H_2O system obtained by the numerical DSMC simulation (the pore phase is rendered as transparent and the red phase is the solid electrode). The mean velocity of H_2 molecules is much larger than that of H_2O, which is attributed to the higher intrinsic diffusion coefficient due to the lower molecular weight and diameter. The application of DSMC method on the reconstructed 3D volume of the electrode effectively addressed the challenge of integrating locally varied Knudsen number into the mass transport simulation and the influence of surface roughness on the gas flow. Accordingly, the Knudsen tortuosity factor τ_k obtained by solving the Knudsen diffusivity in Eq. (7) based on the gas flux from DSMC simulation, and the apparent permeability k_k obtained by ideal gas law and differential form of Darcy's lay (see Eq.(S8) in SI) are expected to be larger compared to the continuum simulation, which often applies the non-slippage boundary condition at the pore-wall boundary and uses viscosity to represent the molecule-molecule interaction.

The Knudsen tortuosity factor of the gas flow pathway as a function of the porosity and pore diameter is evaluated using a series of morphologically dilated pore phase based on the pristine data (Fig. 2f), with the green phase representing the percolated pore network and red phase representing the isolated pores. The percolation ratio is 99.1% at ε = 19% and even higher as the porosity increases. Fig. 2g compares the Knudsen tortuosity factor τ_k (red scatter points) with the values obtained by continuum flow physics τ_c (black scatter points). It is found that τ_k is more than two times larger than τ_c (25.3 *vs.* 12.3). This disparity decreases with the increase in porosity and pore diameter. This is what we would expect because the role of Knudsen effect is weakened with the increase in pore diameter, making the diffusivity less dependent on the diffusing gas species and conditions (i.e. pressure, temperature etc). Likewise, the apparent permeability taking into account the wall-molecule interaction for different porosity samples are summarised in Table 2. The Knudsen tortuosity factors τ_k for different porosity samples are used for the electrochemical simulations in the next section.

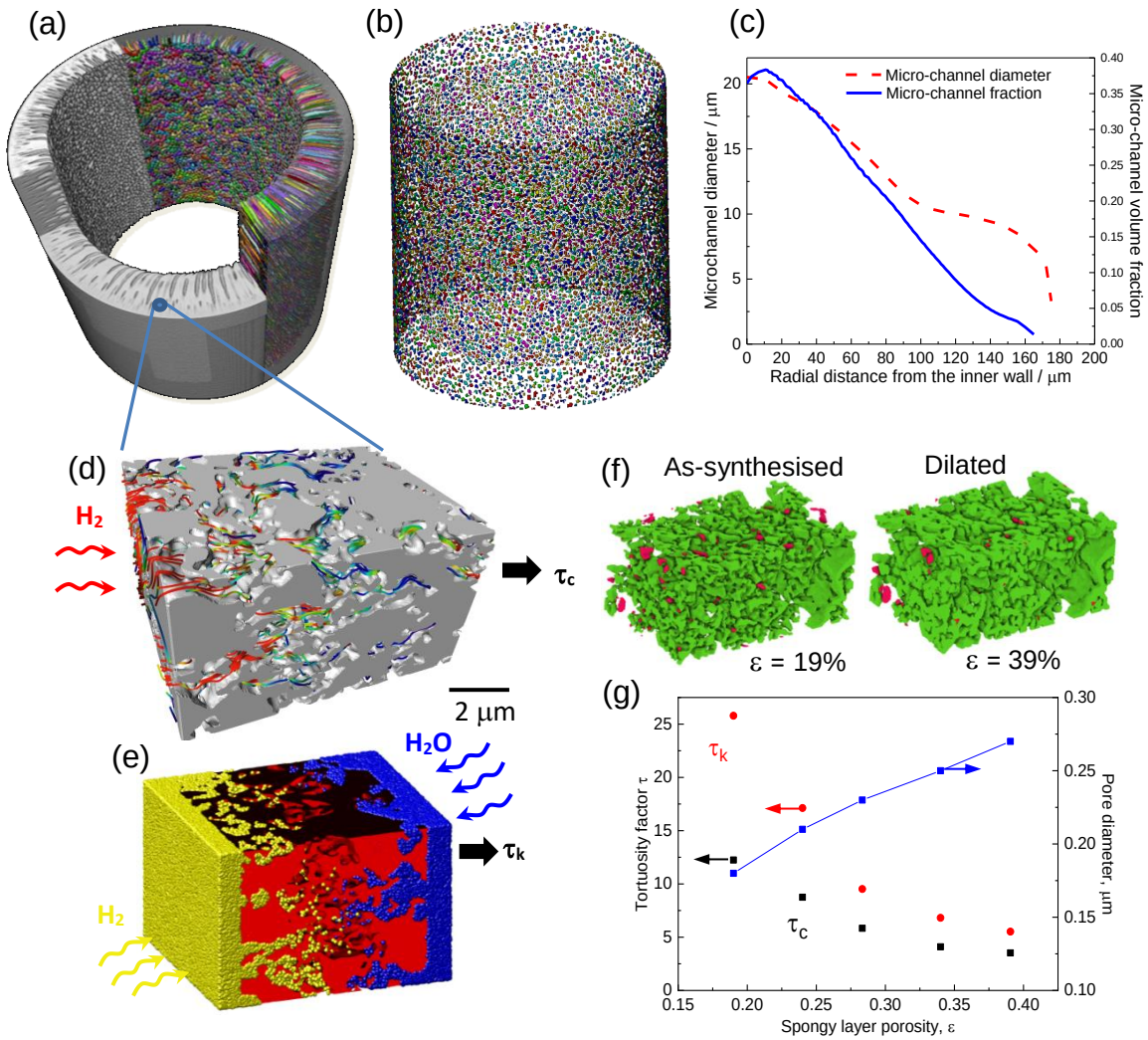

Fig. 2 Characterisations of the 3D porous microstructure at multi-length scale in the MT-SOFC. (a) Macroscopic visualisation of the 3D distribution of the micro-channels; (b) extracted cross-sections of the micro-channels on concentric layers along radial direction; (c) measured micro-channel size and volume fraction distributions along the radial direction based on the cross-sections in (b); the extraction of continuum tortuosity factor τ_c and Knudsen tortuosity factor τ_k based on the reconstructed anode substrate using (d) H_2 diffusion simulation with continuum physics and (e) H_2/H_2O counter diffusion simulation using non-continuum DSMC method respectively. The solid phase is rendered as grey and red in (d) and (e). The pore phase is rendered transparent; (f) porosity obtained from as-synthesised sample was used as the 'seed' to conduct morphological operation so as to obtain a series of pore structures with different porosities and pore diameters for the

parametric study. Red phase represents the isolated pores; (g) comparisons of the Knudsen and continuum tortuosity factor τ_k and τ_c as a function of the porosity and pore diameter.

Table 2 Apparent permeability (k_k) obtained by DSMC simulation

Porosity	19 %	24 %	28 %	34 %
Permeability (m^2)	5.7×10^{-16}	7.1×10^{-16}	8.5×10^{-16}	9.8×10^{-16}

4.2 Electrochemical Simulations

The confidence of the obtained effective mass transport parameters was confirmed by conducting a representative volume element (RVE) analysis (See Section 3 in SI). The result shows that the porosity and tortuosity factor converge at 70% and 60% of the sample volume used in the study. This also corroborates that the homogenised mass transport property of the sponge layer used in the macro-scale model is valid as the length scale of the local pore heterogeneity is small compared to the sample volume we used. The electrochemical simulation was also substantiated by the simulated electrochemical performance (V-I curve) with the experiment data for different characteristic microstructures of MT-SOFC at various operating temperatures (See Section 4 in SI). It appeared to be a decent agreement for the majority of the simulated current density range. This proves that the effective mass transport parameters obtained via computed fluid dynamics (CFD) simulation based on the 3D reconstructed microstructure can provide reliable electrochemical performance prediction using the physics-based model developed in this study. It is intuitive to see the electrode with percolated micro-channels performs significantly better than the one with non-percolated design and its maximum power density (0.98 W cm^{-2}) is significantly higher than the conventional design (0.4 $\sim$ 0.6 W cm^{-2}) [7-9]. This substantiates the efficacy of micro-channels in enhancing the mass transport from the MT-SOFC geometric configuration.

Since the electrochemical performance of the energy device depends on both the thermodynamics properties of the electrodes (e.g. exchange current density), and the mass transport parameters such as percolation, tortuosity and constrictivity of the pore phase, the same microstructural variation could have a positive impact on the reaction kinetics but negative influence on the mass transport. It is of great importance to understand the effect of the microscopic material parameters both parametrically and collectively. The effect of micro-channel morphologies (e.g. geometry, density) and the relative importance compared to the microscopic parameters in the spongy layer in determining the global performance will also be discussed in the following study.

4.2.1 Parametric Study 1: effect of micro-channel length

The effect of micro-channels length on the mass transport and thus electrochemical performance is investigated first. The simulations were conducted on geometric configurations with different micro-channel lengths, ranging from 0% to 95% of the anode thickness, while the properties in the spongy substrate are maintained constant as as-synthesised (Fig. 3). Different micro-channel lengths can be achieved by using different types of bore fluids [16-18] during fabrication.

Fig. 3 shows that at current density i = 2 A cm^{-2}, the sample 0%L without micro-channels shows serious H_2 depletion, which is slightly mitigated in 40%L sample, although the difference is not large as the H_2 partial pressure at the reacting site is still below 0.2 bar, much lower than those with the micro-channels no shorter than 75% of the anode thickness (above 0.7 bar). As a consequence, significant concentration overpotentials are observed in 0%L and 40%L samples but not in the other two cases (see the third panel from the top in Fig. 3). This substantiates the efficacy of micro-channels in enhancing the mass transport from the MT-SOFC geometric configuration. In addition, a smooth gradient of the concentration overpotential distribution is observed ahead of the tip of the micro-channels (and across the entire 0%L sample) while the concentration overpotential is insignificant within the spongy volume between the micro-channels. This phenomenon is a consequence of fast replenishment of H_2 diffusing from the neighboring micro-channels, as indicated

by the H_2 partial pressure map and the insertion of the mass flux vectors surrounding the micro-channels in Fig. 3. The extent of different polarisation mechanisms (activation, concentration, ohmic) can be distinguished as reported in the lower panel of Fig. 3: by deactivating the mass transport physics (i.e. only initial concentration state was used), the influence of the concentration polarisation can be isolated; likewise, by further increasing the exchange current density i_0 up to infinity the activation polarisation can be identified. The polarization curves in the last row of Fig. 3 clearly show serious H_2 starvation for 0% and 40%L samples, as evidenced by the 'bent' of the concentration potential loss (red line), but are not visible for the 75% and 95%L samples. As the length of micro-channel increases, the electrochemical performance is more heavily limited by the activation loss. It is also noted that the accessible maximum current density increases with the micro-channels. All of these substantiate the efficacy of micro-channels in the improvement of mass transport and thus electrochemical performance.

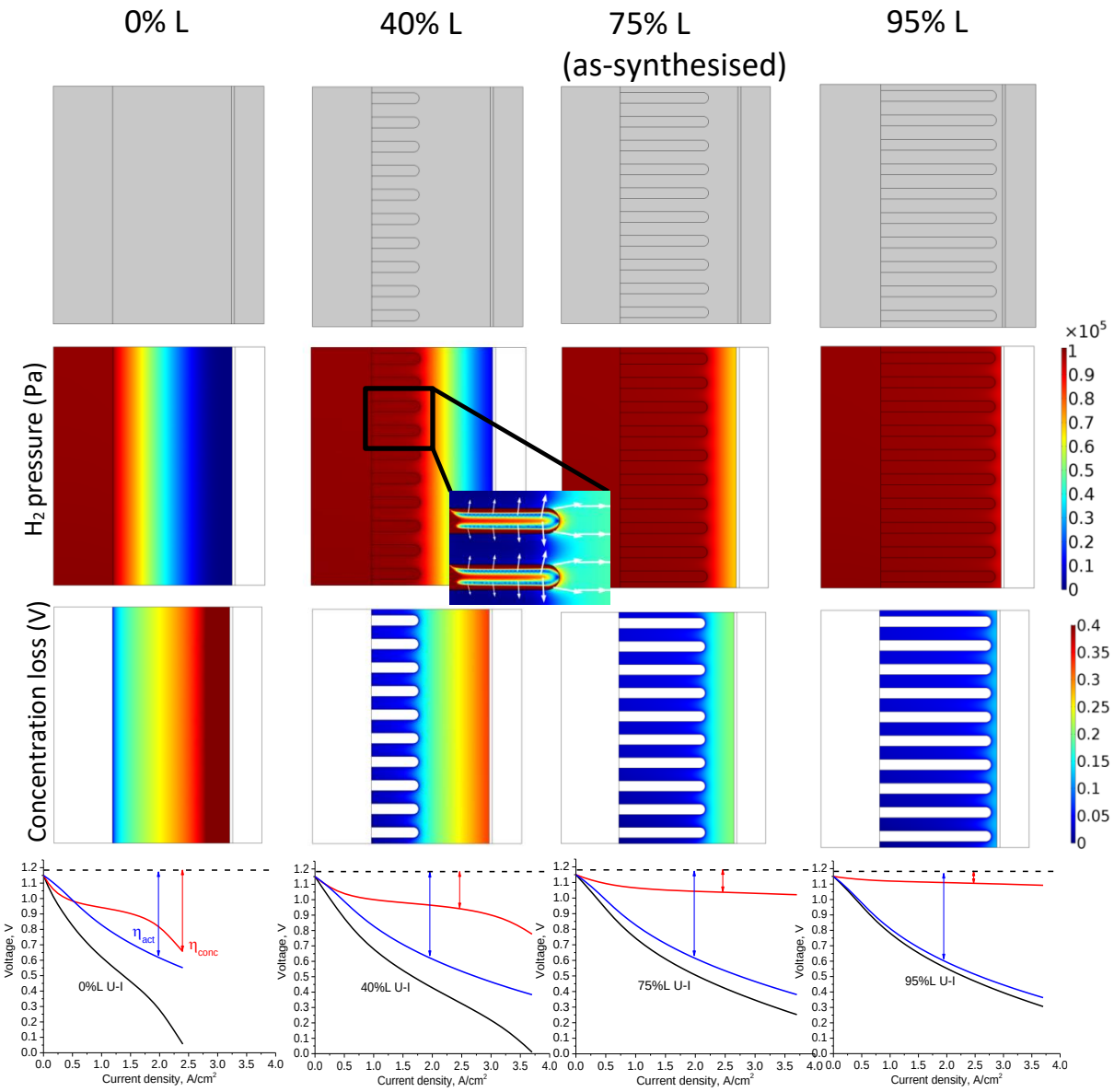

Fig. 3 Parametric study of the effect of micro-channels length on the mass transport and electrochemical performance. The insertion of 40%L sample shows the mass flux vector field surrounding the micro-channels.

The concentration overpotentials as a function of the current density under different micro-channel lengths are plotted in Fig. 4a. It shows that when the micro-channels length is below 60% of the anode thickness, the curves sharply incline at high current density regime, indicating the H_2 starvation caused by the sluggish mass-transport. This phenomenon not only limits the

electrochemical performance of the cell, but also undermines the integrity of the anode microstructure due to H_2 starvation, thus affecting the long-term stability [55]. It is also noted that when the micro-channels is longer than 75% of the anode thickness, the concentration overpotential can be suppressed to less than 0.1 V for current densities up to 4 A cm^{-2}.

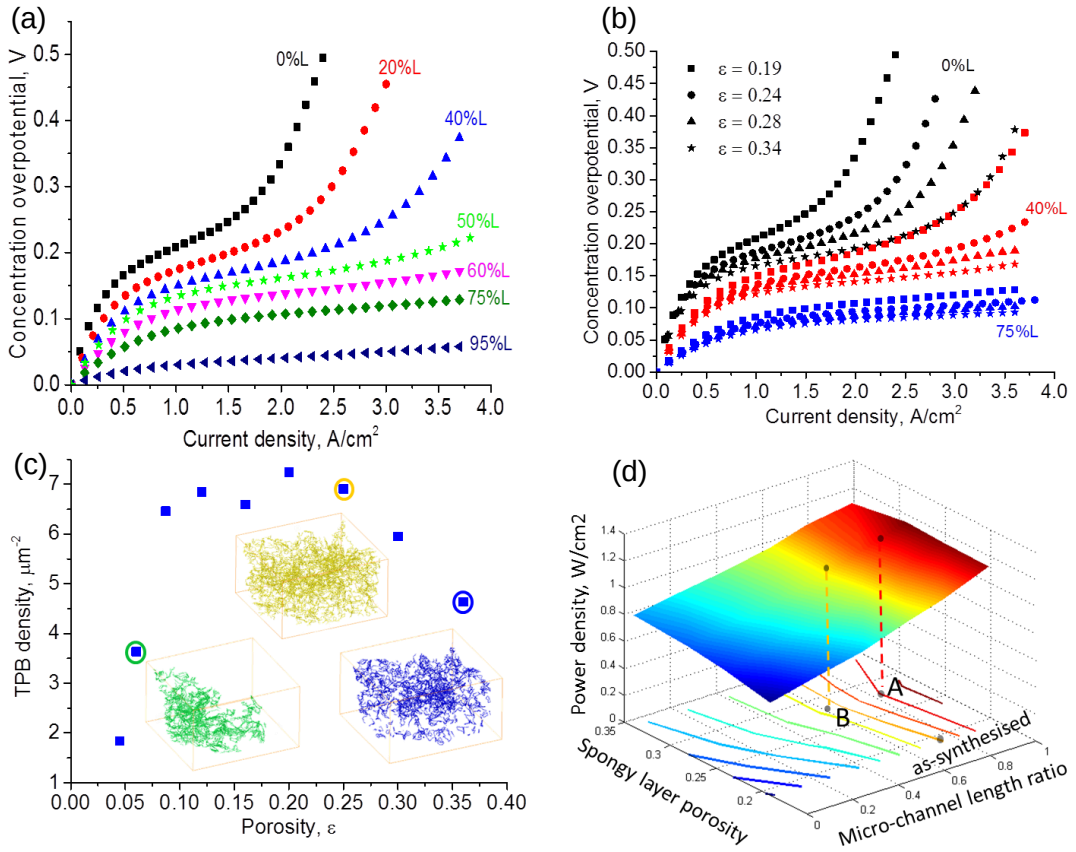

Fig. 4 Concentration overpotential as a function of the current density for (a) the geometries of different micro-channel length ratios and (b) different spongy substrate porosities. After taking into account the (c) TPB density dependence on the substrate porosity, the power density as a function of both spongy substrate porosity and micro-channel length is plotted in (d). Point A indicates the anode design with high power density but at the expense of shorter life time compared to point B, which is a more balanced design strategy. The as-synthesised sample is also shown as a reference.

4.2.2 Parametric Study 2: effect of anode porosity and pore diameter

The effect of porosity (pore diameter) is subsequently investigated. Fig. 4b plots the concentration overpotentials as a function of the current density for anodes of different porosities. It shows that the porosity of the substrate plays an important role in the mass transport in the samples of short micro-channels length. For instance, there is a remarkable disparity between the curves of different porosities for the 0%L sample. As for 40%L, the difference decreases with the increase of substrate porosity and no obvious difference is seen in the 75%L sample, where the concentration overpotential is almost independent of the spongy layer porosity. This suggests that the impact of porosity is significant only when the mass transport process is not dominated by the micro-channels, which is assumed to be at the length of 60% anode thickness based on the observation in Fig. 4a. In other words, for micro-channels shorter than 60%L, increasing the spongy layer porosity allows for a significant reduction in concentration losses. In fact, for a 40%L sample, the H_2 starvation can be suppressed by increasing the spongy substrate porosity from 19% to 28%. This guideline can be used as a reference to infer the minimum porosity in order to avoid H_2 starvation in the electrode design. As an example, if micro-channels are manufactured as less than 40% the anode thickness, the minimum porosity of the spongy layer should be higher than 30% and vice-versa. By comparing Fig. 4a and Fig. 4b closely, we find that the performance of 50%L at 19% porosity is equivalent to that of 40%L at 24% porosity, and 60%L at 19% porosity is identical to 40%L at 28% porosity, which are informative in inferring the ideal anode microstructure by balancing the weight of micro-channels and spongy layer porosity to achieve a competitive electrochemical performance while maintaining a high mechanical strength [56].

Apart from the mass transport, the determination of the substrate porosity is also guided by the TPB density [10, 57, 58]. The porosity should be ensured to be no lower than the percolation threshold (10%), but too high porosity not only results in the loss of mechanical strength, but also reduces the TPB density. This is shown in Fig. 4c, where the TPB density increases sharply when the porosity is below 10%, indicating a percolation limiting regime; above the pore percolation threshold, the TPB density reaches a plateau ($\lambda_{TPB} \approx 6.7\ \mu m^{-2}$) and then drops dramatically when the porosity is above

25%. The TPB loss above this point could be caused by the decrease of the Ni/YSZ interfacial area and the number of paired Ni/YSZ particles [10]. Also, the increase in porosity above 30% could undermine the solid phase percolation (percolation threshold approx. 35% vol [59]). The insets in Fig. 4c help the visualization of the change of TPB density as a function of the porosity from the 3D distribution of the TPBs.

By integrating all these materials characteristics into the model, the predicted power density of the MT-SOFC is plotted as a function of both porosity and micro-channel length (Fig. 4d). It can be seen that the maximum power density (1.18 W cm^{-2} at 95%L, 24% $\sim$ 28% porosity) is ca. 70% higher than the minimum one corresponding to the conventional tubular design (0.59 W cm^{-2} at 0%L, 19% porosity). Moreover, the projected contours become flatter relative to the spongy substrate porosity with the increase in micro-channel length, suggesting the weakened impact of porosity for micro-channels longer than 60%L as described above. It is noted that the power density distribution is quasi-symmetrical to ε = 27%. The power density loss at high porosity regime is attributed to the TPB loss whereas at low porosity regime it results from the poor mass transport property. The two interceptions of the power density contours with the symmetrical axis (ε = 27%) indicate two options for the electrode manufacturing: Point A could be the design for the energy applications prioritising high volumetric power density (1.18 W cm^{-2}) where the mechanical strength is not the limiting factor, whereas Point B is a more balanced choice to ensure an ideal power density (0.96 W cm^{-2}) while maintaining mechanical (flexure) strength above the suggested value 150 MPa, according to the experimental results reported before [18]. It is seen that the as-synthesised sample falls within the limits of these two designs.

4.2.3 Parametric Study 3: effect of different micro-channel geometries

A parametric study of the effect of different geometries the micro-channels on the gas transport and thus electrochemical performance will provide insightful knowledge on the further improvement of the micro-tubular structure. Apart from the length of the micro-channels, which was already illustrated in the previous section, the contribution of other micro-channel metrics such as width, percolation, compactness and radial distribution is discussed here. Firstly, the effect of micro-channels width is investigated parametrically (6, 12 and 24 μm), as shown in Fig. 5. It displays that the H_2 molar flux in the micro-channels is much higher than that in the spongy substrate. Surprisingly, there is no visible difference of the H_2 mole fraction distributions between the three cases. This means that the overall mass transport property is practically independent of the width of the micro-channels. This is explained by looking at the molar flux maps: the molar flux is inversely proportional to the width of the micro-channels. The tips of the micro-channels function like local H_2 supply sources to the reaction sites, and the disadvantage of narrower micro-channels is compensated by faster mass transport, driven by a larger concentration gradient from the entrance to the tip of the micro-channels.

Moreover, the geometric configuration with the micro-channels internally embedded in the substrate (i.e., disconnected from the center bore) is also investigated (Fig. 6). This geometry corresponds to the MT-SOFC fabricated using polyvinyl alcohol solution (PVA, non-solvent) as bore fluid, resulting in a low entrance diameter of the micro-channels (1 ~ 2 μm) [18, 60]. It is found that the H_2 mole fluxes in the micro-channels are significantly lower than those obtained in open micro-channels in Fig. 5, but there is no noticeable difference of the mole flux in the spongy substrate. The molar flux vectors from the inset display that the H_2 molecules are drawn from the spongy anode into the micro-channels and diffuse outward at the tip of the micro-channels. These closed micro-channels can still act as mass transport fast tracks, although the H_2 repletion is sluggish due to the disconnection to the center bore. As a consequence, the H_2 fraction is lower across the anode substrate compared to the open micro-channels case. Again, there is no difference between

different micro-channels widths as the mole flux increases with the decrease of the micro-channels width, same to the open micro-channel case.

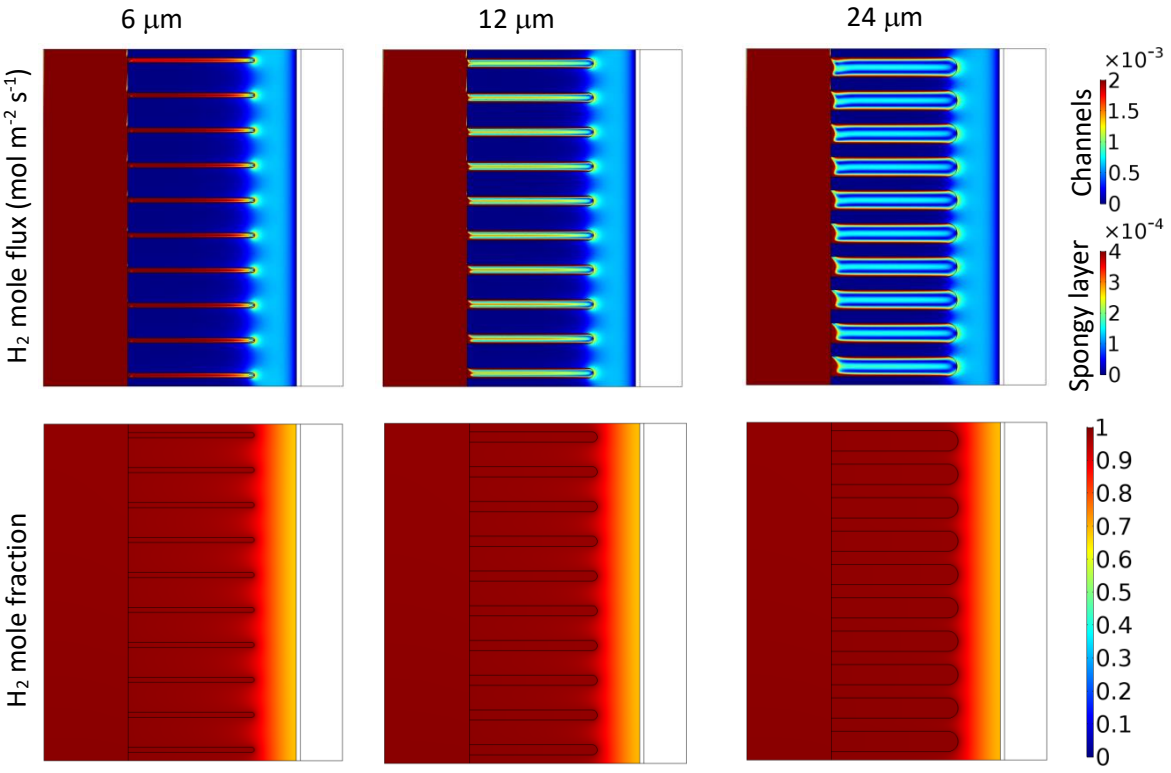

Fig. 5 Reactant transport and distribution simulated on the geometric configurations of different micro-channels width at i = 2 A cm^{-2}.

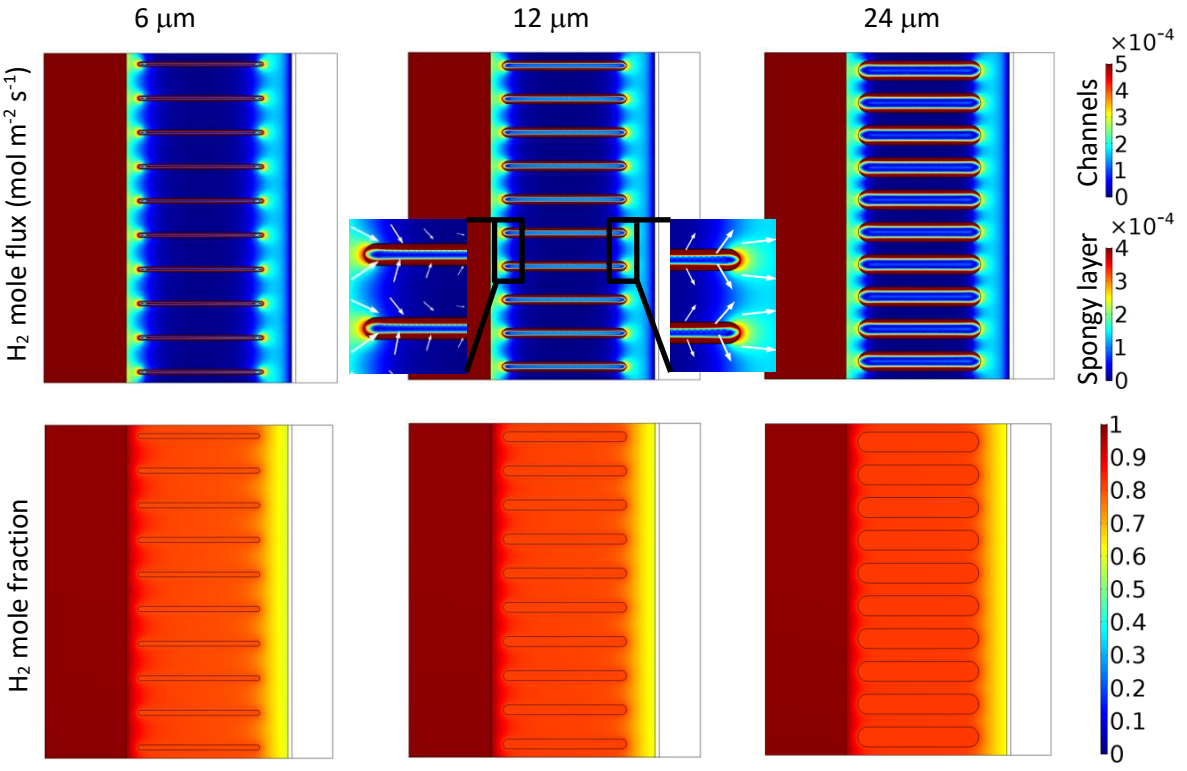

Fig. 6 Reactant transport and distribution simulated on the geometric configurations of different micro-channels width with internally embedded micro-channels at i = 2 A cm^{-2}.

In manufacturing process, the trade-off between mechanical robustness and mass transport is often the prime concern when tailoring the microstructure towards different operating conditions in micro-tubular SOFCs [61-63]. For power density-oriented design, in which the length of the micro-channel cannot be sacrificed, an alternative solution could be the compactness of the micro-channels. The first row of Fig. 7 presents the simulated H_2 mole distribution at i = 2 A cm^{-2} on three types of sample with varied micro-channel compactness. Compared to the as-synthesised sample which is embedded with 10 micro-channels (i.e. Fig. 1g and Fig. 3, 40 μm/channel in longitudinal direction), 1-channel sample (400 μm/channel) exhibits serious heterogeneity of H_2 distribution at the reacting interface due to the uneven delivery rate. In contrast, 3-channels sample (130 μm/channel) effectively mitigates the local variation of the H_2 distribution, which is critical in maximising the reacting area thus the power density as well as preventing uneven degradation of

the anode. 5-channels sample (80 μm/channel) displays similar H_2 transport capability compared to the as-synthesised one. Fig. 8 compares the global performance of the anode design with varied micro-channel compactness. It is observed that there is negligible performance difference between the 5-channels sample and the synthesised one. 3-channels sample is slightly inferior to the former two, while the 1-channel sample displays significant drop of the performance, as the consequence of uneven distribution of the H_2 at the reacting surface, as is shown in Fig. 7. We can safely conclude that the micro-channel compactness of the as-synthesised electrode can be reduced by a factor of two to three without a notable drop of the power density. It needs to be pointed out that, the effect of compactness (or number density) discussed here is independent of the width of the micro-channels, because the narrow micro-channels can provide as much gas flux as the wider ones due to the larger reactants gradient, as was illustrated earlier. However, given the identical compactness to ensure the homogeneous reactant distribution at the electrolyte/anode interface, wide micro-channels detrimentally reduce the mechanical robustness which is critical for the durability of the cell pack.

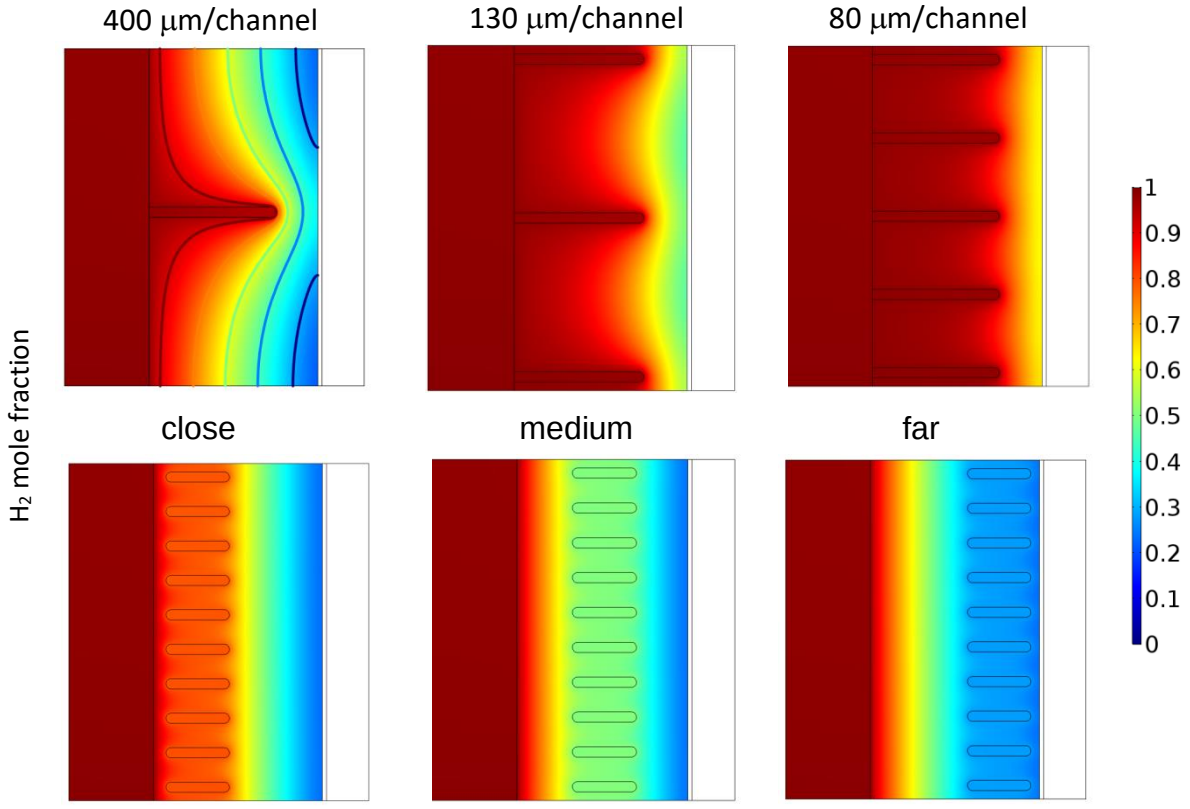

Fig. 7 The effect of micro-channel compactness and radial distribution on the H_2 mass transport in terms of mole fraction distribution at i = 2 A cm^{-2}.

Finally, the effect of radial arrangement of the micro-channels is discussed, which is aligned with the interest of designing porosity-graded SOFC anode [64, 65]. The second row in Fig. 7 shows that the H_2 distribution is greatly dependent on the radial location of the micro-channels. The embedment of micro-channels significantly increases the local mass transport and as a consequent, the gradient of H_2 mole fraction is remarkably suppressed in the micro-channel region. However, the H_2 distribution is identical in the three cases at the anode/electrolyte interface, combined with the evidence of similar performance in Fig. 8, we can conclude that the global H_2 delivery of the micro-tubular structure is not affected by the radial arrangement of the micro-channels, although it facilitates the local mass transport, the electrochemical performance is speculated to be mainly governed by the sub-micron pores in the substrate instead of the micro-channels. However, they still show much better performance than the conventional substrate free of any micro-channels, as is shown in Fig. 8. If the micro-channels are percolated from the inner wall of the tube and extend at least 60% of the radial distance, the mass flux at the reacting interface will be mainly determined by the micro-channels instead of the micro-pores in the substrate, as was discussed in Section 4.2.1. As the control over the asymmetric structure of the micro-tubular SOFC and the formation mechanisms of the micro-channels were well studied [56, 66, 67], the fundamental understanding of the efficacy of the microstructures at multi-length scale in this work will provide insightful information towards the practical structural design in manufacturing.

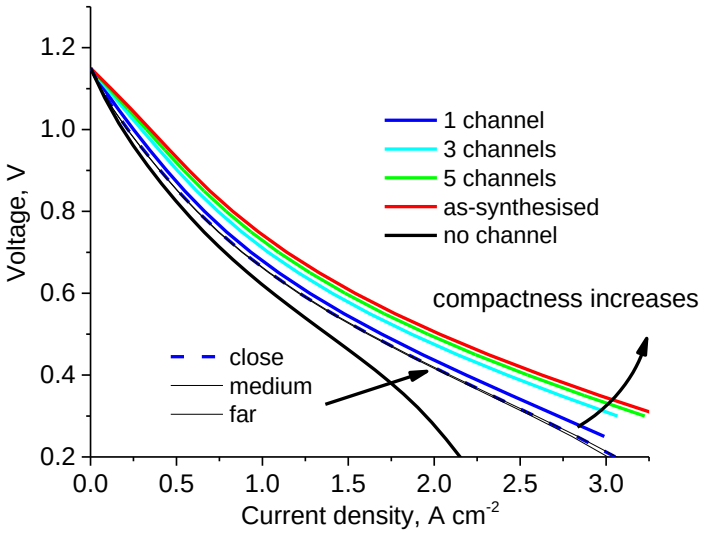

Fig. 8 Comparisons of the effect of micro-channel compactness and radial distribution on the global performance.

5. Conclusion

In this study, in order to guide the synthesis of the optimised electrode, we have investigated the effect of each individual microstructural characteristics on the electrochemical performance of the micro-tubular SOFC fabricated by phase-inversion technique. We first evaluated the effective mass transport parameters as a function of the porosity and pore diameter of the anode substrate for both the continuum flow (viscous diffusion) and non-continuum flow (Knudsen diffusion) respectively. A molecule-based Direction Simulation Monte Carlo (DSMC) method was applied to the 3D reconstructed porous microstructure of the anode to account for the molecule/surface collisions. It is found that the Knudsen tortuosity factor reaches 25.3 for the as-synthesised sample (19% porosity, pore diameter 0.18 μm), which is approximately two times larger than the tortuosity factor for the continuum flow (12.3). With the increase of the porosity and pore diameter, the disparity of these two values becomes less significant, which is attributed to the weakened Knudsen effect and less tortuous gas pathways.

The electrochemical performance at different temperatures predicted by 2D simulation incorporating the obtained effective mass transport parameters showed good agreement with the experimental results. Parametric studies show that micro-channels length should be no less than 60% of the anode thickness in order to eliminate the H_2 depletion at the reaction sites, which would otherwise undermine the microstructural stability of the anode and limit the electrochemical performance. The impact of porosity and pore diameter on the global mass transport is insignificant as long as the micro-channels length reaches at least 60% of the anode thickness. We also find that the improvement of mass transport arising from 10% longer micro-channels length can be compensated by 5% lower anode porosity when the micro-channels is less than 60% of the anode thickness. For those applications prioritising the maximum power density (1.18 W cm^{-2}), the MT-SOFC could be manufactured with 80% of the micro-channel radial occupation and 27% porosity, while 60% micro-channels length and 27% porosity can provide a more balanced performance in terms of power density (0.96 W cm^{-2}) and long-term structure integrity. This information can be helpful when modifying the substrate porosity for an improved TPB density or for enhanced mechanical strength.

The width of the micro-channels should not be a concern in the material manufacturing as it actually has little effect on the mass transport and, in turn, on the electrochemical performance. The compactness of the micro-channels greatly affect the homogeneity of the reactants distribution at the electrolyte/anode interface, and it is found that 80 μm/channel (even 130 μm/channel) can provide identical performance as the current 40 μm/channel design, but with improved mechanical robustness. If not being percolated from the inner wall, the radial arrangement of the micro-channels has no effect on the global electrochemical performance of the cell, although it significantly improves the local mass transport capability, in which case the improvement of the substrate porosity and pore size should be aimed for.

The significance of this study lies not only in suggesting sensible microstructural characteristics to improve the MT-SOFC performance, but also improves knowledge of the impact from each individual microstructural parameters and their potential correlation can provide more possibilities towards advanced anode design. This work will be of significant interest to the readership, not only those engaged with fuel cell research, but also the wider energy materials community such as batteries, membranes and catalysts which integrate hierarchical porous structure to facilitate the mass transport, due to the wide applicability of the developed methodology.

Acknowledgement

The authors acknowledge support from the EPSRC under grants EP/M014045/1, EP/P009050/1 and EP/N032888/1. Paul R Shearing acknowledges funding from the Royal Academy of Engineering. Antonio Bertei acknowledges funding from the innovation programme under the Marie Skłodowska-Curie grant agreement No. 654915 and the European Union's Horizon 2020 research.

References

[1] Y. Wu, J.I.S. Cho, X. Lu, L. Rasha, T.P. Neville, J. Millichamp, R. Ziesche, N. Kardjilov, H. Markötter, P. Shearing, D.J.L. Brett, Journal of Power Sources, 412 (2019) 597-605.
[2] Y. Wu, J.I.S. Cho, T.P. Neville, Q. Meyer, R. Ziesche, P. Boillat, M. Cochet, P.R. Shearing, D.J.L. Brett, Journal of Power Sources, 399 (2018) 254-263.
[3] C. Hatchwell, N. Sammes, K. Kendall, Journal of power sources, 70 (1998) 85-90.
[4] I.P. Kilbride, Journal of Power Sources, 61 (1996) 167-171.
[5] T. Suzuki, Z. Hasan, Y. Funahashi, T. Yamaguchi, Y. Fujishiro, M. Awano, Science, 325 (2009) 852-855.
[6] N. Akhtar, S. Decent, D. Loghin, K. Kendall, Journal of power sources, 193 (2009) 39-48.
[7] D. Panthi, A. Tsutsumi, Scientific reports, 4 (2014) 5754.
[8] N.-Q. Duan, D. Yan, B. Chi, J. Pu, L. Jian, Scientific reports, 5 (2015).
[9] L. Zhou, M. Cheng, B. Yi, Y. Dong, Y. Cong, W. Yang, Electrochimica Acta, 53 (2008) 5195-5198.
[10] X. Lu, T.M.M. Heenan, J.J. Bailey, T. Li, K. Li, D.J.L. Brett, P.R. Shearing, Journal of Power Sources, 365 (2017) 210-219.
[11] S.M. Jamil, M.H.D. Othman, M.A. Rahman, J. Jaafar, A.F. Ismail, K. Li, J. Eur. Ceram. Soc., 35 (2015) 1-22.
[12] K. Li, Ceramic membranes for separation and reaction John Wiley & Sons Ltd, Chichester, UK, 2007.
[13] T. Li, Z. Wu, K. Li, J. Power Sources, 273 (2015) 999-1005.
[14] H. Strathmann, K. Kock, Desalination, 21 (1977) 241-255.
[15] S. Liu, Ceram. Int., 29 (2003) 875-881.

[16] T. Li, X. Lu, B. Wang, Z. Wu, K. Li, D.J. Brett, P.R. Shearing, Journal of Membrane Science, 528 (2017) 24-33.
[17] X. Lu, O.O. Taiwo, A. Bertei, T. Li, K. Li, D.J.L. Brett, P.R. Shearing, Journal of Power Sources, 367 (2017) 177-186.
[18] M.H.D. Othman, Z. Wu, N. Droushiotis, G. Kelsall, K. Li, Journal of Membrane Science, 360 (2010) 410-417.
[19] M. Morales, M. Laguna-Bercero, RSC Advances, 7 (2017) 17620-17628.
[20] Z. Han, Z. Yang, M. Han, International Journal of Hydrogen Energy, 41 (2016) 10935-10941.
[21] C. Yang, C. Jin, F. Chen, Electrochemistry Communications, 12 (2010) 657-660.
[22] X. Lu, B. Tjaden, A. Bertei, T. Li, K. Li, D. Brett, P. Shearing, Journal of The Electrochemical Society, 164 (2017) F188-F195.
[23] L. Salvo, M. Suéry, A. Marmottant, N. Limodin, D. Bernard, Comptes Rendus Physique, 11 (2010) 641-649.
[24] E. Maire, P. Withers, International materials reviews, 59 (2014) 1-43.
[25] J. Veldsink, R. Van Damme, G. Versteeg, W. Van Swaaij, The Chemical Engineering Journal and the Biochemical Engineering Journal, 57 (1995) 115-125.
[26] A. Borner, F. Panerai, N.N. Mansour, International Journal of Heat and Mass Transfer, 106 (2017) 1318-1326.
[27] S. Jaganathan, H. Vahedi Tafreshi, B. Pourdeyhimi, Chemical Engineering Science, 63 (2008) 244-252.
[28] R. Jambunathan, D.A. Levin, A. Borner, J.C. Ferguson, F. Panerai, International Journal of Heat and Mass Transfer, 130 (2019) 923-937.
[29] C. White, T.J. Scanlon, R.E. Brown, Journal of Spacecraft and Rockets, 53 (2015) 134-142.
[30] L.M. De Socio, L. Marino, Journal of Fluid Mechanics, 557 (2006) 119-133.
[31] T. Oshima, S. Yonemura, T. Tokumasu, in: AIP Conference Proceedings, AIP, 2012, pp. 809-815.
[32] Y. Nakano, S. Iwamoto, I. Yoshinaga, J.W. Evans, Chemical Engineering Science, 42 (1987) 1577-1583.
[33] J.M. Zalc, S.C. Reyes, E. Iglesia, Chemical Engineering Science, 59 (2004) 2947-2960.
[34] A. Bertei, B. Nucci, C. Nicolella, Chemical Engineering Science, 101 (2013) 175-190.
[35] X. Lu, T. Li, A. Bertei, J.I.S. Cho, T.M.M. Heenan, M.F. Rabuni, K. Li, D.J.L. Brett, P.R. Shearing, Energy & Environmental Science, (2018).
[36] X. Lu, T. Li, A. Bertei, J.I.S. Cho, T.M.M. Heenan, M.F. Rabuni, K. Li, D.J.L. Brett, P.R. Shearing, Energy & Environmental Science, 11 (2018) 2390-2403.
[37] J. Schindelin, I. Arganda-Carreras, E. Frise, V. Kaynig, M. Longair, T. Pietzsch, S. Preibisch, C. Rueden, S. Saalfeld, B. Schmid, Nature methods, 9 (2012) 676-682.
[38] M.A. Gallis, J.R. Torczynski, S.J. Plimpton, D.J. Rader, T. Koehler, AIP Conference Proceedings, 1628 (2014) 27-36.
[39] Z.-X. Sun, Z. Tang, Y.-L. He, W.-Q. Tao, Computers & Fluids, 50 (2011) 1-9.
[40] C. Shu, X. Mao, Y. Chew, International Journal of Numerical Methods for Heat & Fluid Flow, 15 (2005) 827-841.
[41] S.J. Cooper, T. Li, R.S. Bradley, K. Li, N.P. Brandon, J.A. Kilner, ECS Transactions, 68 (2015) 1857-1864.
[42] E.N. Fuller, P.D. Schettler, J.C. Giddings, Industrial & Engineering Chemistry, 58 (1966) 18-27.
[43] B. Todd, J.B. Young, Journal of Power Sources, 110 (2002) 186-200.
[44] P.-W. Li, M.K. Chyu, Journal of Power Sources, 124 (2003) 487-498.
[45] N.F. Bessette, W.J. Wepfer, J. Winnick, Journal of the Electrochemical Society, 142 (1995) 3792-3800.
[46] H. Zhu, R.J. Kee, Journal of Power Sources, 117 (2003) 61-74.
[47] H. Iwai, N. Shikazono, T. Matsui, H. Teshima, M. Kishimoto, R. Kishida, D. Hayashi, K. Matsuzaki, D. Kanno, M. Saito, H. Muroyama, K. Eguchi, N. Kasagi, H. Yoshida, Journal of Power Sources, 195 (2010) 955-961.

[48] D.G. Goodwin, H. Zhu, A.M. Colclasure, R.J. Kee, Journal of The Electrochemical Society, 156 (2009) B1004-B1021.
[49] B. Boer, SOFC anode: hydrogen oxidation at porous nickel and nickel/zirconia electrodes, Universiteit Twente, 1998.
[50] A. Bertei, J. Mertens, C. Nicolella, Electrochimica Acta, 146 (2014) 151-163.
[51] B. Kenney, K. Karan, Solid State Ionics, 178 (2007) 297-306.
[52] H. Zhu, R.J. Kee, Journal of the Electrochemical Society, 155 (2008) B715-B729.
[53] H. Zhu, R.J. Kee, V.M. Janardhanan, O. Deutschmann, D.G. Goodwin, Journal of the electrochemical society, 152 (2005) A2427-A2440.
[54] T. Tsai, S.A. Barnett, Solid State Ionics, 93 (1997) 207-217.
[55] T. Parhizkar, R. Roshandel, Energy Conversion and Management, 133 (2017) 20-30.
[56] N. Yang, X. Tan, Z. Ma, Journal of Power Sources, 183 (2008) 14-19.
[57] W. Zhu, D. Ding, C. Xia, Electrochemical and solid-state letters, 11 (2008) B83-B86.
[58] T.M.M. Heenan, J.J. Bailey, X. Lu, J.B. Robinson, F. Iacoviello, D.P. Finegan, D.J.L. Brett, P.R. Shearing, Fuel Cells, 17 (2017) 75-82.
[59] D. Bouvard, F. Lange, Acta metallurgica et materialia, 39 (1991) 3083-3090.
[60] K. Kanawka, M.H.D. Othman, N. Droushiotis, Z. Wu, G. Kelsall, K. Li, Fuel Cells, 11 (2011) 690-696.
[61] B.R. Roy, N.M. Sammes, T. Suzuki, Y. Funahashi, M. Awano, Journal of Power Sources, 188 (2009) 220-224.
[62] P. de Wit, F.S. van Daalen, N.E. Benes, Journal of Membrane Science, 524 (2017) 721-728.
[63] N. Droushiotis, U. Doraswami, K. Kanawka, G. Kelsall, K. Li, Solid State Ionics, 180 (2009) 1091-1099.
[64] P. Holtappels, C. Sorof, M. Verbraeken, S. Rambert, U. Vogt, Fuel Cells, 6 (2006) 113-116.
[65] M. Ni, M.K.H. Leung, D.Y.C. Leung, Journal of Power Sources, 168 (2007) 369-378.
[66] M.H.D. Othman, Z. Wu, N. Droushiotis, G. Kelsall, K. Li, Journal of Membrane Science, 360 (2010) 410-417.
[67] C.C. Wei, K. Li, Industrial & Engineering Chemistry Research, 47 (2008) 1506-1512.